PNAS RESEARCH ARTICLE | APPLIED PHYSICAL SCIENCES OPEN ACCESS

Multilayered optofluidics for sustainable buildings

Raphael Kay[a,b,c,1], J. Alstan Jakubiec[c,d], Charlie Katrycz[a], and Benjamin D. Hatton[a,1]

Edited by Howard Stone, Princeton University, Princeton, NJ; received June 16, 2022; accepted November 13, 2022

Indoor climate control is among the most energy-intensive activities conducted by humans. A building facade that can achieve versatile climate control directly, through independent and multifunctional optical reconfigurations, could significantly reduce this energy footprint, and its development represents a pertinent unmet challenge toward global sustainability. Drawing from optically adaptive multilayer skins within biological organisms, we report a multilayered millifluidic interface for achieving a comprehensive suite of independent optical responses in buildings. We digitally control the flow of aqueous solutions within confined milliscale channels, demonstrating independent command over total transmitted light intensity (95% modulation between 250 and 2,500 nm), near-infrared-selective absorption (70% modulation between 740 and 2,500 nm), and dispersion (scattering). This combinatorial optical tunability enables configurable optimization of the amount, wavelength, and position of transmitted solar radiation within buildings over time, resulting in annual modeled energy reductions of more than 43% over existing technologies. Our scalable "optofluidic" platform, leveraging a versatile range of aqueous chemistries, may represent a general solution for the climate control of buildings.

dynamic building facade | microfluidics | smart windows | energy efficiency | active optics

Buildings are the costliest energy sinks on the planet (1, 2). For their daily operation, which largely entails trying to heat, cool, and light the indoor environment as exterior conditions change, buildings require 32% (32.4 PWh) of the energy and 50% of the electricity consumed globally (2), corresponding to about 25% (9.18 $GtCO_2$) of our greenhouse gas emissions (1).

Moreover, the emissions associated with buildings may double or triple by mid-century with increased urbanization (1). Global air conditioning demand is set to triple by 2050 (3). Heating and cooling energy use is expected to grow by 79% and 84% in the same timeframe (1). In addition, electricity-based emissions from residential and commercial buildings have already quintupled and quadruped, respectively, in the last four decades (1).

Underpinning this alarming and growing footprint is a fundamental unmet challenge in building design: existing facades cannot achieve selective, reconfigurable responses to their solar environment; no window, sunshade, or chromogenic technology is able to independently tune the amount (intensity), wavelength (spectrum), and dispersion (scattering) of incident sunlight as solar conditions change (a comprehensive review of available technologies and their optical properties is provided in *SI Appendix*, Table S1).

Static windows, with or without permanent reflective coatings, for instance, cannot dynamically modulate solar intensity, spectrum, nor scattering (4–6). Manual or automated venetian blinds, on the other hand, can partially control intensity and scattering (with changing slat angle), but not independently (7). Adjustable window shades, which can be bent, rotated, or otherwise translated under mechanical (6, 8–12), electrical (13), hygroscopic (14, 15), or thermal (16) stimuli, can usually tune only total intensity (17), while more experimental chromogenic windows, including reorientable liquid crystal (18–20), suspended particle (21–23), as well as electro- (24–34), photo- (26, 28, 29, 31, 35), and thermochromic (26, 28, 29, 31, 35–37) devices, can generally only regulate total sunlight intensity or spectrum (32–34, 38).

At the building interface, independent, synergistic control over transmitted light intensity, spectrum, and scattering is necessary to achieve optimized and climate-responsive functions (4, 6, 31, 39). Control of total light intensity would enable modulation of solar heat gain and illumination; control of spectrum and, in particular, switchable transmission of near-infrared-selective (NIR) sunlight would decouple infrared heating from visible daylighting (38, 40); while control of scattering would allow for the spatial tuning of transmitted photons within a room. In the current absence of a building material with this combinatorial functionality, interior heating, cooling, and lighting systems must bear the brunt of temperature and illumination control, compensating entirely for exterior environmental fluctuations and interior occupant changes, and by themselves consume more than 25% of the energy used in the developed world (4, 6, 31, 39, 41).

Significance

Buildings consume 32.4 PWh (32%) of our global energy supply, a footprint that is expected to double by mid-century. Designing facades like the skins of biological organisms, with dynamic multilayered optical reconfigurability, would enable homeostasis-like environmental responsiveness and significantly improved energy efficiency. Here, we develop an adaptive building interface, leveraging confined multilayered fluids to achieve a versatile library of shading, scattering, and selectively absorbing solar responses. Configurable optimization of this "building-scale microfluidic" platform can reduce energy consumption in our models by 43%, representing a design paradigm toward net-zero buildings.

Author affiliations: [a]Department of Materials Science and Engineering, University of Toronto, Toronto, ON M5S 3E4, Canada; [b]Department of Mechanical and Industrial Engineering, University of Toronto, Toronto, ON M5S 3G8, Canada; [c]John H. Daniels Faculty of Architecture, Landscape, and Design, University of Toronto, Toronto, ON M5S 2J5, Canada; and [d]School of the Environment, University of Toronto, Toronto, ON M5T 1P5, Canada

Author contributions: R.K. and B.D.H. designed the research; R.K. performed experiments; J.A.J. developed the model; C.K. contributed to experimental design; R.K. and J.A.J. analyzed data; R.K. wrote the paper; and R.K, J.A.J., C.K., and B.D.H. edited the paper.

The authors declare no competing interest.

This article is a PNAS Direct Submission.

[1]To whom correspondence may be addressed. Email: raphael.kay@mail.utoronto.ca or benjamin.hatton@utoronto.ca.

This article contains supporting information online at https://www.pnas.org/lookup/suppl/doi:10.1073/pnas.2210351120/-/DCSupplemental.

Published January 30, 2023.

To alter this energy-intensive paradigm (41), buildings would benefit from independent, switchable control over total transmittance, NIR-selective absorption, and scattering by the outer facade. Developing this scalable, combinatorial optical platform, with the ability to separately tune each of these three properties, might be considered the "holy grail" for building material design (42).

Multilayered Optical Mechanisms in Biology. As a possible source of inspiration, certain biological organisms have evolved multilayered mechanisms within their skin to tune independent optical properties at their interface. In a few species of squid (e.g., *Loligo plei*), for instance, active camouflage is achieved through the independent and cooperative action of a pigmentary layer of chromatophore organs and a structural layer of protein cells (43–45), mediating surface color, spectral reflectance, and spatial patterning (46–50) (Fig. 1*B*). Large shifts in spectral reflection peaks occur along surface regions where both pigmentary and structural layers are overlaid (*SI Appendix*, Fig. S3 *C–J*), enabling combinatorial, additive, optical responses. The panther chameleon has also evolved a multilayered infrastructure within its skin, leveraging a two-tiered system of photonic crystals, each with an independent morphology and function (51) (Fig. 1*A*). Color change is regulated through the uppermost photonic layer, as chameleons actively manipulate the periodicity of guanine nanocrystals to selectively reflect light. Thermoregulation, on the other hand, is achieved through the lowermost photonic layer, where populations of regularly arranged iridophore cells strongly reflect radiation in the NIR region.

Independently tunable and multifunctional multilayer interfaces enable combinatorial physiological responses in organisms. We hypothesize that building-scale analogues of these multilayered, multifunctional biological systems might be capable of similarly dynamic optical behaviors (*SI Appendix*, Fig. S3). To achieve a scalable and sustainable material platform with general optical tunability, we propose moving away from traditional solid-state approaches and instead suggest the integration of confined aqueous fluids: a class of replenishable, recyclable, nontoxic materials with remarkable spatial configurability (54–57) and broadly tailorable optical programmability (58, 59). Conventional microfluidic devices are typically applied to chemical (60, 61), diagnostic (62, 63), and computational (64, 65) "lab on a chip" applications, but few examples take advantage of the optical characteristics of confined fluids, and over large planar dimensions. We suggest that a system of stacked channeled layers capable of confining a selectively designed collection of fluids can achieve versatile, multifunctional, and combinatorial optical functionality.

Here, we demonstrate a large-area "optofluidic" platform for buildings, capable of achieving independent and combinatorial control of total light transmission, spectrally selective light absorption, and spatially directable light dispersion through coordinated digital fluid flows therein (Fig. 1 *C–E*). In simulation, we show that independent control over three sequential aqueous fluid layers within a building facade—to regulate optimal degrees of total light transmission, NIR light transmission, and visible light scattering in response to fluctuating solar conditions—can accomplish savings of 75% on heating energy, 20% on electric lighting energy, and 43% on total operational energy, compared with the best available electrochromic technology. These results point toward an exciting design paradigm for buildings, where confined, switchable fluid layers within a facade can behave in concert as functionally programmable optical and solar filters. Dynamic control of this versatile fluidic platform could significantly improve the way we build, operate, and interact with buildings.

Results

Functional Fluidic Optical Controls. We fabricated bilayer and trilayer devices (15 × 15 × 2 cm^3) from polymethylmethacrylate (PMMA) sheets (3 mm thick) with millimeter-scale channels for fluid flow (1.5 mm deep, 6.35 mm wide) (Fig. 2*B*). Multilayers were designed with stacked parallel-channel architectures, and the ends of each channel structure were connected to fluid reservoirs (14 mL). Digital syringe pumps were used to flow (15 mL/min) aqueous solutions into and out of the channels, to demonstrate switchable and reversible control over visible-selective and NIR-selective absorption, total transmission, and scattering (Fig. 1*B*). Devices could achieve a transparent state when filled with a liquid [mineral oil, 1.48 refractive index (RI)] with a similar RI to PMMA (1.49) (*SI Appendix*, Fig. S2).

Additive selective absorption. In multilayered devices, overall color can be controlled with combinations of dyed solutions, using established color theory (66). When two fluid layers overlap, we should expect the transmission spectrum through the bilayer to equal the product of the transmission spectra of the layers independently (66). We demonstrated this effect by flowing two spectrally selective fluids within parallel layers of a bilayer device (blue and yellow dye solutions, with absorption peaks at 630 nm and 430 nm, respectively) (Fig. 2 *A–C*, *i–iv*). In series, these layers transmitted light with an effective green color (absorption peaks at 630 and 430 nm), as the measured (combined) spectrum closely matched the theoretical curve (Fig. 2 *C*, *vi*). We demonstrated a wide range of color control by activating combinations of aqueous yellow, orange, red, green, and blue dyes (*SI Appendix*, Fig. S4 *A* and *B*). Expected changes to absorption spectra and overall color were achieved across the device (209 cm^2) using only 14 mL of solution (0.067 mL/cm^2) within 40 s of channel-filling (*SI Appendix*, Fig. S4*C*).

Dynamic NIR-selective absorption. Developing scalable materials capable of independently regulating visible and NIR sunlight has been considered the most important challenge in building design (42). In practice, however, NIR transmission through modern windows is typically fixed below 50% using static low-emissivity (67) and spectrally selective (68) window coatings. An energetically optimal window, instead, should toggle between high and low transmission states, depending on fluctuating outdoor solar availability and indoor solar requirement (69).

Because many liquids are strongly absorbing in the NIR (750 to 2,500 nm), but transparent within the visible (350 to 750 nm), we suggest that confined fluid flows can achieve selective switchable control over NIR absorption within a window transparent to visible light. We tested a series of fluids and solutions that are transparent (>75%) in the visible but highly absorbing in the NIR within a bilayer device. Air is transparent across the visible and NIR spectrum (350 to 2,500 nm); glycerol absorbs frequently in the NIR (absorbance peaks at ~1,200 nm, ~1,400 nm, and ~1,700 nm) and completely between 2,250 and 2,500 nm; while highly diluted aqueous carbon black pigment (0.0156 mg carbon/mL) absorbs completely between 1,400 and 2,500 nm (Fig. 2*E*). When we replace an air layer with this aqueous pigment, for instance, the visible transmission through the device is reduced only mildly (ΔT_{vis} = 16%); however, the transmitted NIR decreases considerably (ΔT_{NIR} = 76%). NIR absorption within the channels is clearly detected (as "effective temperature") by an IR camera (Fig. 2*D*).

To demonstrate the impact of this active NIR switching on interior temperature, we developed a simple scaled-down room model (30 × 30 × 30 cm^3), clad on one side with a single-layered (15 × 15 cm^2, 1.5-mm channel depth, 14 mL volume) fluid device (Fig. 2*G*). We exposed the "room" externally with a 100-W

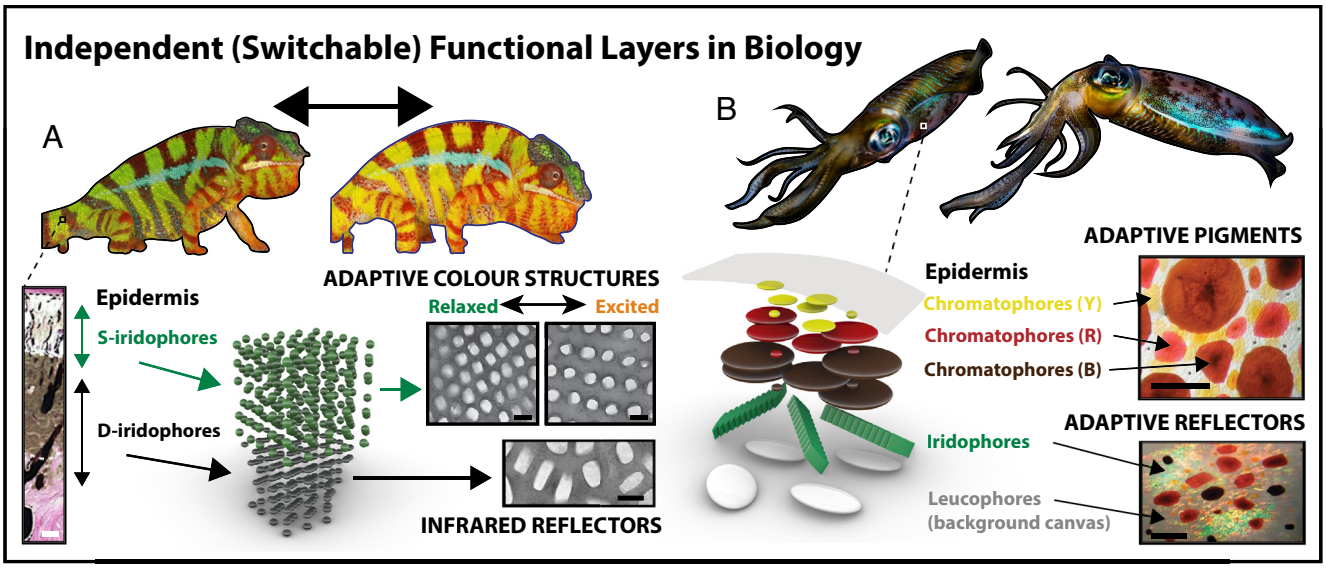

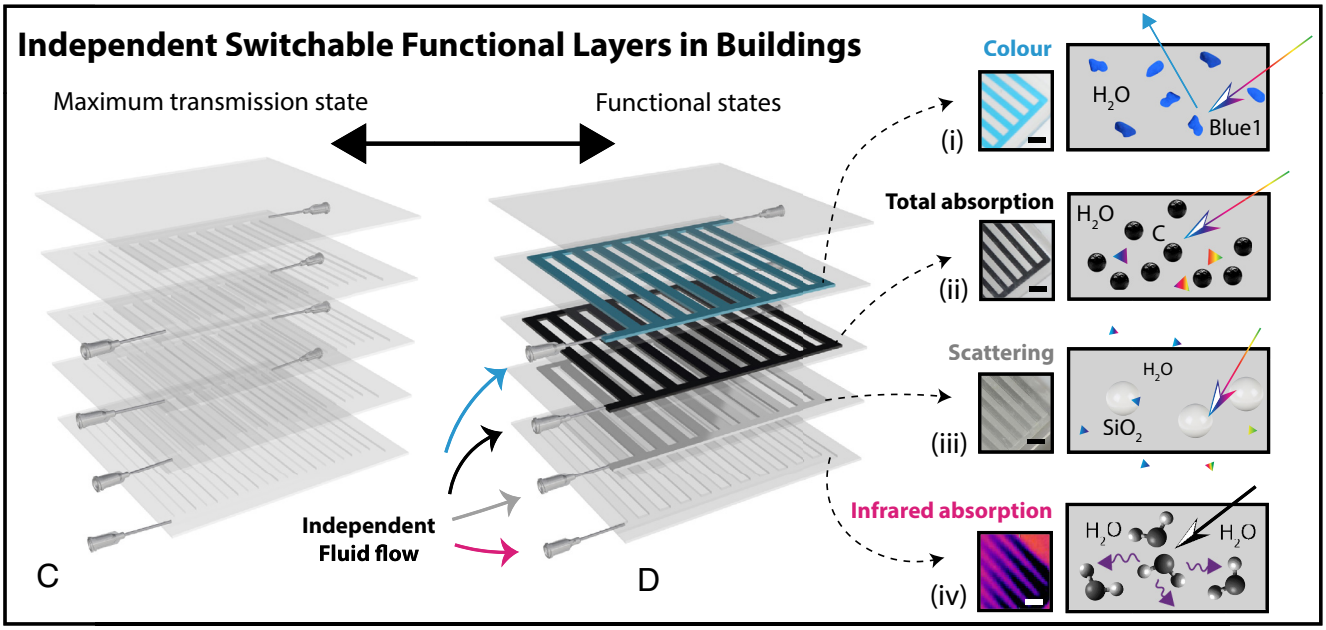

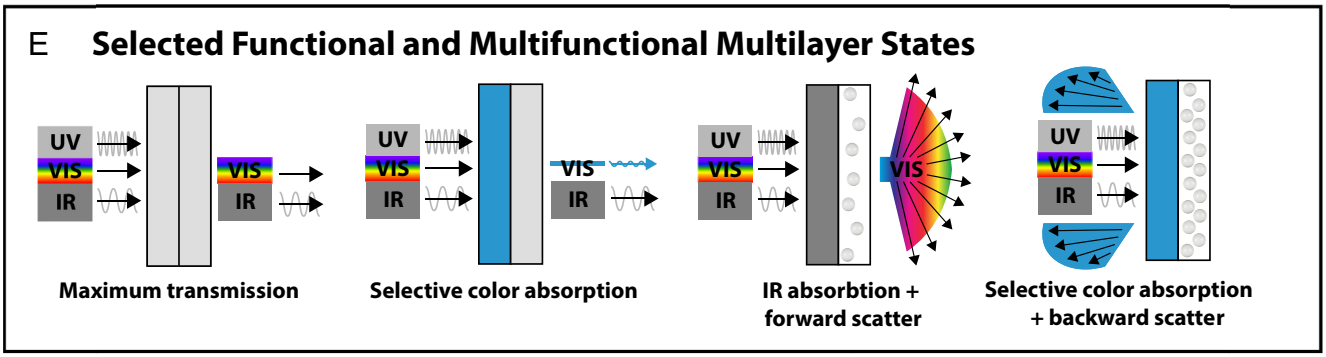

Fig. 1. Biological inspiration for fluidic multilayer. (*A*) Color change in the panther chameleon, achieved using a multilayer architecture of active photonic crystals. (*B*) Color change in the squid, achieved using coordinated actuations within a multilayer of pigmentary and structural elements. The top images are of *Sepioteuthis lessoniana*, whereas the bottom images are of *Loligo pealeii*. (*C* and *D*) Schematic for achieving independent multilayered switchable responses in building facades, where switchable fluid flow within distinct layers can enable multiple distinct optical functions. (*E*) Schematic exemplifying several functional or multifunctional states, achieved through coordinated fluid injections within a bilayer. The fluid multilayer acts as an additive light filter for incoming light. Scale bars: (*A*) white, 20 μm; black, 200 nm; (*B*) 1 mm; (*D*) 1 cm. Images in (*A*) reproduced from ref. 51, published under a Creative Commons license (http://creativecommons.org/licenses/by/4.0/). Images in (*B*) reproduced with permission from ref. 48, and under license from refs. 52 and 53.

incandescent bulb until an interior thermocouple (on a PMMA support) reached a steady state (39 °C after 30 min, *Materials and Methods*). We then injected aqueous pigment within the device, to absorb a substantial portion of the incident NIR. This caused the interior thermocouple to cool to 32 °C within 15 min, while the device remained transparent in the visible (Fig. 2*F*). This

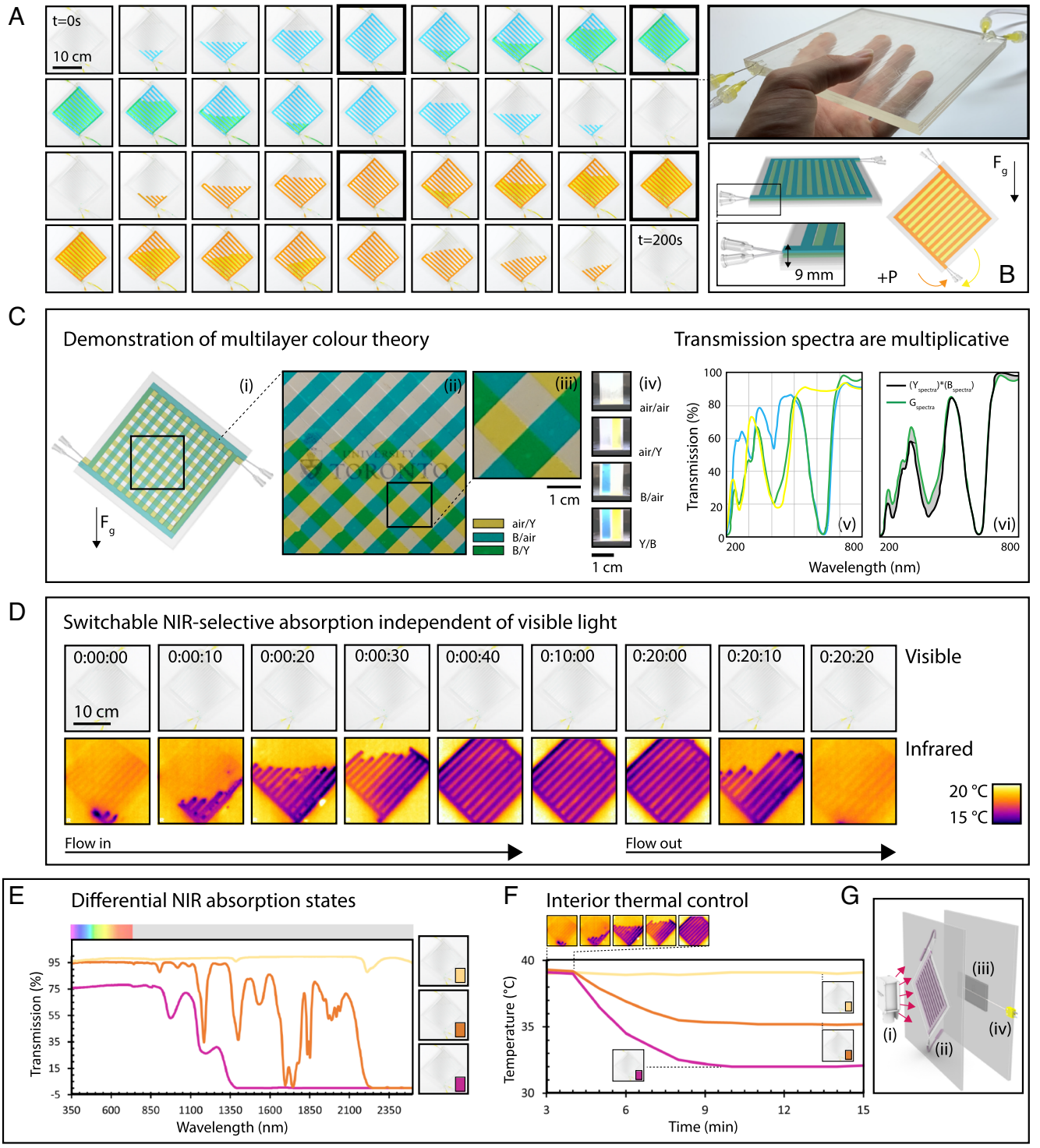

Fig. 2. Additive and spectrally selective absorption. (*A*) Still frames across two complete cycles of fluid injection and retraction, demonstrating four unique colored states (bolded frames) within fluidic devices. Photograph of bilayer device shown to demonstrate device scale and visible transparency. Fluids were cycled up to 100 times within channel layers, with no evidence of fouling. (*B*) Design of bilayer device. (*C*) Overlapping crosshatch bilayer design, demonstrating periodic instances of additive color filtering, as well as instances of single-layer color filtering. Spectral measurements (v) were taken using "model" bilayer sample section, shown in (iv), and illustrate transmission spectra from both independent layers (yellow, blue) and combined bilayer (yellow and blue). We confirm that transmission spectra are multiplicative, where B/Y bilayer spectrum [green curve in (vi)] is equivalent to multiplication of B spectrum and Y spectrum [black curve in (vi)]. (*D*) Aqueous fluid injection and retraction sequence, from left to right, imaged in the visible and IR spectrum (with a digital camera and infrared (IR) camera, respectively). While there are no noticeable changes to visible transmission, IR transmission is decreased with fluid injection, and increased again with fluid retraction. Experiment conducted in the horizontal plane for ease. The timestamps are formatted as hours:minutes:seconds. (*E*) Differential NIR transmission across three independent fluids (air, glycerol, and 0.0156 mg carbon/mL water, from top to bottom) that each have high transmission in the visible spectrum. (*F*) Temperature of PMMA plate behind a fluid layer across an injection sequence of each fluid from (*E*). Air represents control injection. (*G*) Experimental schematic for temperature measurements in (*F*). (i) 100-W incandescent light bulb as heat source. (ii) switchable fluid layer. (iii) PMMA plate. (iv) thermocouple measuring PMMA temperature over time. Other experimental details can be found in *Materials and Methods*.

simple fluidic system represents a window material with state memory [i.e., can maintain state without constant energy input (42, 70)] capable of independently tuning NIR and visible light transmittance—a significant advance in building technology (42).

Dynamic transmission and shading. The ability to actively modulate the transmission of solar radiation for control over interior light intensity is a crucial function for energy conservation. If large-area switchable shading could be consistently achieved, models suggest that annual operational energy consumption of buildings could be reduced by up to 50% (71). Here, we injected aqueous suspensions of carbon black pigment (paracrystalline carbon) within a bilayer device to modulate total light transmission (Fig. 3 *A*–*C* and Movie S1). When the device was mounted along one wall of a model enclosure (30 × 30 × 15 cm^3), we could measure interior light intensity using a photovoltaic light sensor (setup in *SI Appendix*, Fig. S6). This physical "room" model allowed us to characterize total transmitted visible light for various pigment concentrations. Importantly, we demonstrated maximum reductions in interior light intensity of 100% when the layers (1.5 mm deep) were completely filled with carbon suspensions of at least 4 mg/mL (Fig. 3*D*). Light transmission within the visible spectrum was spectrally uniform and, as expected, intensity decreased with particle concentration of shading fluids (Fig. 3*E*).

The Beer–Lambert law (72) (Eq. 1) determines the absorbance (ratio of incident I_0 to transmitted I intensity) through each fluid layer as a function of molar absorptivity ε, the layer thickness b, and particle concentration c. In agreement with this model, absorbance of our aqueous layers was linearly proportional to its pigment concentration (Fig. 3*E*). We verified this using Eq. **1** to calculate the expected transmission spectra for various aqueous pigment

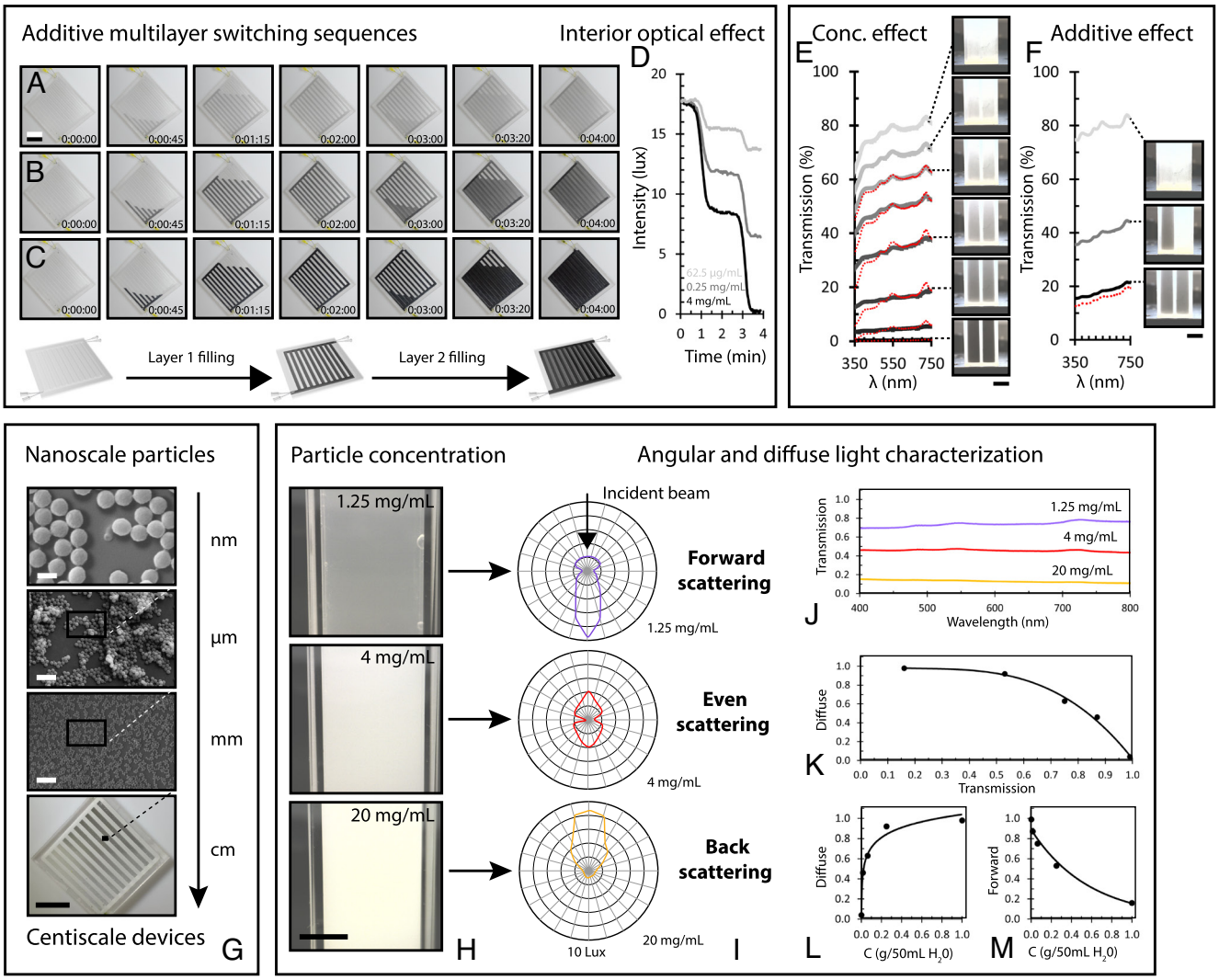

Fig. 3. Dynamic fluidic shading and scattering. (*A*–*C*) Still frames across three independent injection sequences within a bilayer, for three fluids of different particle concentrations (concentrations in *D*). (Scale bar is 5 cm.) The timestamps are formatted as hours:minutes:seconds. (*D*) Corresponding interior light intensity measurement within model room (experiment demonstrated in *SI Appendix*, Fig. S6). (*E*) Measured transmission spectra (within cuvette) as function of particle concentration. Curves correspond to transmission spectra of fluids concentrated at 0, 15.6, 21.5, 30.0, 44.5, 77, 130, and 250 µg C/mL H_2O, from top to bottom. Spectral information into the NIR range is available in *SI Appendix*, Fig. S11. (*F*) Measured transmission spectra (within cuvette) as function of number of activated (filled) layers. Dotted red lines show Beer–Lambert model estimate, calculated from the measured transmission spectrum of the 15.6 µg/mL solution using Eq. **1**. Images show cross-section of bilayer cuvette. Fluid concentrated at 77 µg C/mL H_2O. Top curve represents spectrum of empty cuvette. Dotted red line shows Beer–Lambert model estimate for completely filled bilayer, calculated by doubling optical path length of spectrum for half-filled bilayer in Eq. **1**. (*G*) SEM and digital images illustrating multiscale fluidic mechanism, utilizing nanoscale particle features for macroscale optical control. Scale bars, from top to bottom, are 4 µm, 2 µm, 250 nm, and 5 cm. Particles in top image are synthesized PMMA. (*H*) Images of three cuvettes, each filled with an aqueous suspension of titania. (Scale bar is 5 mm.) (*I*) Differentially scattered light profiles for each fluid concentration in (*H*). Increasing concentrations correspond to increasing back scattering. Data is plotted on a logarithmic scale. (*J*) Suspensions with higher particle concentrations transmit less visible light. Curves represent specular transmission measurements. (*K*–*M*) Suspensions with higher particle concentrations scatter more visible light (*L*). Therefore, as transmission increases, relative scattered (diffuse) lighting decreases (*K*), representing a limit to the degree of independence between transmission and scattering.

solutions (dotted red curves in Fig. 3*E*) from a known transmission spectrum and concentration (15.6 μg/mL), finding close agreement with our measured spectra. We also verified that absorbance was linearly proportional to the depth (optical path length) of our fluid layers, measuring reductions in transmitted light intensity in agreement with Eq. **1** when we activated a second shading fluid layer behind the first, effectively doubling b (Fig. 3*F*, dotted red curve).

$$\log_{10}\frac{I_0}{I} = \varepsilon bc. \qquad [1]$$

With both color and intensity control established, we also demonstrated additive color and "dimming" by activating both a switchable color layer and switchable absorbing layer (*SI Appendix*, Fig. S5 and Movie S2).

Dynamic scattering. The ability to modulate light intensity can be augmented by the ability to additionally modulate the distribution of light intensity, for controlling the area over which a fixed number of photons are spread. In buildings, light scattering might reduce excessively lit areas, increase the depth of daylight penetration, and improve the overall quality of illumination, which reduces electric lighting demands and improves human health and productivity (73, 74). Moreover, control of scattering might enable tunable spatial daylighting within a room, as occupancy density and distribution fluctuates over time. To date, however, only mechanical blinds are able to dynamically control light scattering to any limited extent. We hypothesize that flow control over colloidal suspensions of titania (TiO_2) nanoparticles can be leveraged to achieve more advanced, controllable Rayleigh scattering at a building scale.

The relative number of photons scattered forward or backward by a nanoparticle in solution can be designed for using the size parameter, $x = 2\pi r \cdot m_0 / \lambda$, where r is the spherical particle radius, m_0 is the RI of the surrounding fluid, and λ is the wavelength of incident light with respect to vacuum (75). P25 titania particles ($r \approx 10$ nm) in aqueous solution, for instance, will scatter visible light within the Rayleigh regime, resulting in a roughly even proportion of photons scattered forward and backward (Fig. 3*H*) (76).

Within this Rayleigh regime, to verify another dimension of control over spatial light scattering, we injected aqueous suspensions of P25 titania (*Materials and Methods*) at various concentrations within a millifluidic bilayer (Fig. 3*H*). We focused an incident white light-emitting diode (LED) source (14 klm normal to the device surface, average λ = 550 nm) to measure the light intensity distribution as a function of concentration (Fig. 3 *H–I*) (77, 78). As predicted, visible light transmission decreased with particle concentration (Fig. 3*J*), while the fraction of transmitted light scattered increased with particle concentration (Fig. 3*L*)—a scattering phenomenon for colloids first explained by Lord Rayleigh (77, 78). This relationship does represent a functional limit to using particles of this size: as light transmission increases, the ability to scatter light decreases (Fig. 3 *K–M*), accordingly bounding the maximum degree of independence between visible light transmission and scattering. However, this adaptive fluidic approach can be applied to scatter visible light in the Mie regime ($r > 30$ nm), for achieving disproportional scattering in the forward direction (75, 76). The components of these suspensions, both particle size and fluid, can therefore be selected to design for a desired pattern of spatial light scattering within a room.

Building-Scale Illumination and Energy Consumption Modeling. A well-established suite of interior daylight and temperature modeling tools allows us to accurately predict how our fluidic materials can improve the performance of buildings. We leveraged both a backward optical raytracing simulator, Radiance (79), and a transient thermal modeler, EnergyPlus (80), to predict how both the static and dynamic performance of our devices could strategically tune the intensity, spectrum, and dispersion of incident sunlight within a digital, computer-designed, interior space. We fed the optical properties corresponding to different measured states of our device into the simulations, providing a link between benchtop-scale optical characterization and building-scale performance prediction.

Simulated interior illuminance with dynamic shading. We used the measured transmission spectra of our devices with different concentrations of aqueous carbon pigment to simulate dynamic shading for a room interior. A well-established backward light-ray-tracing simulator and renderer (Radiance) (79) was leveraged to model diffuse and specular daylight penetration, and compare illuminance across a standard digitally modeled space, clad in a single switchable fluid layer. Luminance, compared across three different concentrations of pigment (Fig. 4*A*), was rendered with six ambient bounces, using weather data from Toronto, Canada, within a conventional two-zone office (*SI Appendix*). Daylight availability was simulated (Fig. 4*B*) within a smaller office (described in ref. 81 and *SI Appendix*).

In our simulations, we demonstrated how light transmission and penetration depth into the digital room was affected by particle concentration, comparing the optical performance of layers with five pigment concentrations (Fig. 4*B*). Annually, as expected, the fraction of interior space conventionally defined as underlit (<100 lux) and partially lit (100 to 300 lux) increased with concentration, while the fraction of space acceptably lit (300 to 3,000 lux) and excessively lit (>3,000 lux) decreased with concentration (Fig. 4 *C–F*). Crucially, we showed that control of our pigment layer can tune the lighting of a whole building interior (Fig. 4 *A–F*).

Simulated interior illuminance and energy consumption with scattering. We used our measured light-scattering results to model luminance across an indoor space (*SI Appendix*) when clad in a control window (no scattering) and in a device-modified window with a single layer of scattering media (4.0 mg TiO_2/mL H_2O, able to scatter 95% of incident light) (Fig. 4 *G–H*)—both with a visible light transmissivity (T_{vis}) of 40%. We calculated daylight availability and found that the fluid layer enables both reduced overlighting (>3,000 lux) in the winter months (low solar altitude) (Fig. 4*I*) and increased light penetration in the summer months (high solar altitude), when compared with the control window (Fig. 4*J*). This scattering allows for annual improvements to optical occupant comfort by increasing daylight autonomy (>300 lux) (Fig. 4*L*) and decreasing the fraction of underlit floor space (<300 lux) (Fig. 4 *M–N*), without compromising excessive daylighting (Fig. 4*K*) (82). With scattering, more daylight is distributed to reflective interior surfaces, and less daylight is absorbed by (lost to) the floor. This increase in useable daylight greatly reduces the need for supplemental electrical lighting deep within the space, leading to annual electric light energy savings of 18% and 9% within room depths of 3 to 6 and 6 to 9 m, respectively (Fig. 4*O*), for a total electric lighting load reduction of approximately 10% (Fig. 4*P*). We envision that colloidal suspension chemistries could also be engineered for broader control of scattering (such as for adjusting relative forward- and backward-dispersion, using particles within the Mie regime), perhaps enabling even greater simulated energy reductions in buildings.

Simulated solar heat gain and energy consumption with dynamic spectrally uniform and spectrally selective shading. Control over visible and NIR light transmission influences interior solar heat gain, defined by the solar heat gain coefficient (SHGC), equal to the fraction of solar radiation admitted through a window at

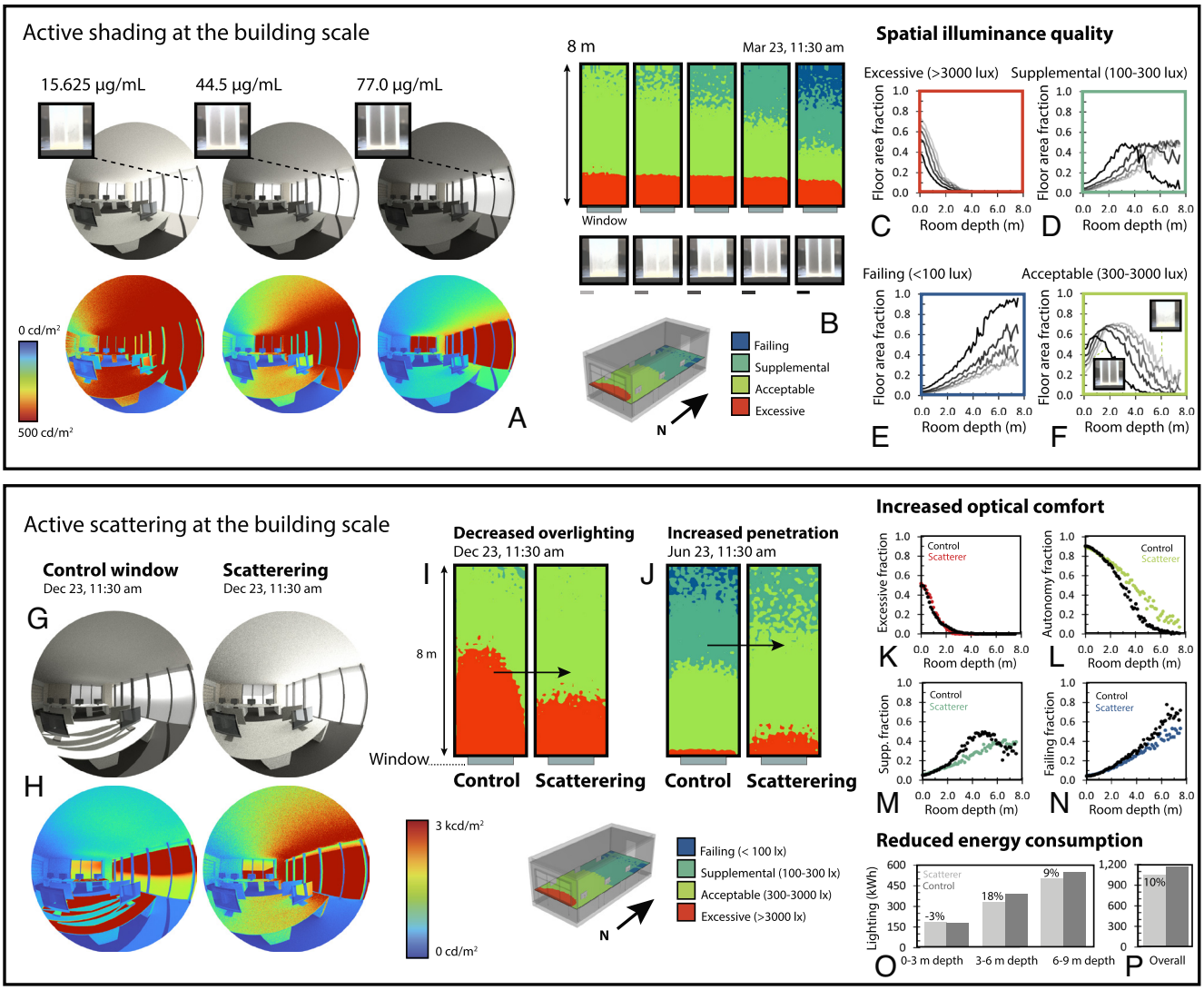

Fig. 4. Simulated indoor daylight tunability. (*A*) Backward ray-tracing renders illustrating daylighting differences for differently concentrated fluid window layers (aqueous carbon black). (*B*) Daylight availability simulations demonstrating differences in available daylight across a modeled interior space for differently concentrated fluid window layers. Window optical properties derived from transmission properties of fluids concentrated at 0, 15.6, 21.5, 44.5, and 77 µg C/mL H_2O, from left to right. Failing, supplemental, acceptable, and excessive daylighting are defined, respectively, as <100 lux, 100 to 300 lux, 300 to 3,000 lux, and >3,000 lux. (*C*–*F*) Floor area fractional spatial illuminance quality for differently concentrated fluid layers as a function of depth within the space. Illuminance values are taken as central (width) value at each depth within the space. Scale bars in (*B*) are 5 mm. (*G* and *H*) Backward ray-tracing renders illustrating spatial daylighting differences between regular control window and window with scattering particles (4 mg TiO_2/mL H_2O). The scattering window enables visibly deeper light penetration. (*I*) Daylight availability simulation demonstrating the degree to which a scattering layer can reduce excessive illuminance. (*J*) Daylight availability simulation demonstrating the degree to which a scattering layer can improve daylight penetration. (*K*–*N*) Scattering layers improve optical comfort, having a small effect on excessive illuminance throughout the year (*K*), but decreasing the fraction of indoor space that requires supplemental electric lighting (*M* and *N*), and increasing the fraction of indoor space that requires no electric lighting (*L*). (*O* and *P*) As a result, the scattering layer enables reductions to electric lighting usage at depths between 3 and 9 m, enabling 10% annual reductions in electric lighting energy consumption.

a fixed incident solar radiation spectrum (83). To demonstrate the impact of active fluidic shading on solar heat gain and building energy efficiency, we used a computational building energy and thermal modeling tool (EnergyPlus) to estimate the annual energy required for heating and cooling a standard space in Toronto. Within our heat-balance model, interior temperature and heat flow were calculated using the conduction finite difference solution algorithm (80, 84) using hourly historical data on outdoor temperature, cloud cover, solar intensity (direct and diffuse radiation) and solar position, while accounting for conductive, convective, and radiative heat flows through, heat storage within, and reemission from, cladding, structural, and indoor materials (more details of model in *SI Appendix*, Tables S2 and S3). For simplicity, we assumed no internal heating loads from lighting, occupants, or equipment.

Practically, we compared heating and cooling for maintaining a constant indoor temperature within the space when clad with i) a static low-emissivity "control" window (SHGC = 0.71; $T_{visible}$ = 0.81; U-value = 1.81 W/m^{2}K), and when additionally clad with ii) our fluid interface that can modulate between a transmitting state (empty air channels) and a fully absorbing state (4 mg carbon/mL water). We also repeated the simulation but with a switchable NIR-selective absorbing fluid state (0.0156 mg carbon/mL water). Operationally, we used a simple control algorithm (56) to instantaneously "inject" the absorbing fluid at hourly timesteps when the interior space needed to be cooled (i.e., when indoor temperature > setpoint temperature). The shading fluid absorbs light that would otherwise be converted to excess heat indoors. We modeled this fluid layer on the outside of the control window and assumed no conductive or radiative heat gain following solar absorption.

In simulation, the absorbing layer was activated during peak solar loading during the day in both winter and summer seasons (operation of layer for sample day demonstrated in Fig. 5*A*, Fig. 5*E*), dramatically decreasing the window solar heat gain and total operational energy requirement (Fig. 5 *C–D, G–H*). Annually, we showed that switchable control of a completely shading fluid (Fig. 5*H*) could reduce the operational energy requirement for indoor space heating and cooling by 51%, exceeding the most ambitious estimates for building energy savings with existing adaptive shading technologies (38, 71). Additionally, we found that the multilayer with active control over only NIR absorption reduced the internal heating and cooling loads by 25% compared with the control window (Fig. 5*D*). This result demonstrates that simple fluid-based systems can decouple NIR and visible light transmission for significant improvements to building efficiency, without compromising daylighting. Going forward, we imagine control algorithms might better optimize these NIR responses, through a 'learned' understanding of the building-specific implications of solar heat transmission (Fig. 5*C*, Fig. 5*G*) on performance (Fig. 5*D*, Fig. 5*H*).

Simulated energy optimization through multilayer tunability. While active control over each of intensity, NIR absorption, and scattering can significantly improve building energy performance, it is the combinatorial control of these independent functions that should enable true configurability and energy optimization. For example, a trilayer fluidic device can switch between a full spectrum of optical states, from transparent, to fully opaque, cloudy, NIR-absorbing, and to any linear combination in between. In Fig. 6*C*, we compare the various "axes" of optical control (visible transmission, NIR transmission, and scattering) for a range of facade technologies. Static glazings (blue square in Fig. 6*C*) allow no control over properties, while conventional dynamic systems [e.g., electrochromic (EC) windows and roller shades (RSs)] allow control over visible and NIR transmission, although dependently (black and gray curves in Fig. 6*C*). Our fluid multilayer is capable of independent control over total absorption, NIR absorption, and scattering across multiple (three) degrees of freedom (pink areas in Fig. 6*C*). Therefore, if we consider each of visible transmission, NIR transmission, and scattering a unique "dimension" of optical control, we might say that static facades are zero-dimensional, conventional dynamic systems including EC windows and RSs are one-dimensional, and, maximally, our fluidic device is three-dimensional.

To estimate the performance of this combinatorial system, we used EnergyPlus to compare the annual energy required to heat, cool, and light our reference space when clad in i) our tunable fluid multilayer, ii) a state-of-the-art EC window, iii) a RS, and iv) a static low-emissivity window. For consistency, we simulated the operation of all dynamic systems using the same control algorithm (Fig. 6*B*), in each case aiming to minimize total energy usage at hourly timesteps, while maintaining a minimum daylight threshold of 300 lux, and limiting overlighting (>3,000 lux) to 10% of the interior space (schematic demonstrating state-switching logic in *SI Appendix*, Fig. S7, other details in *SI Appendix* and

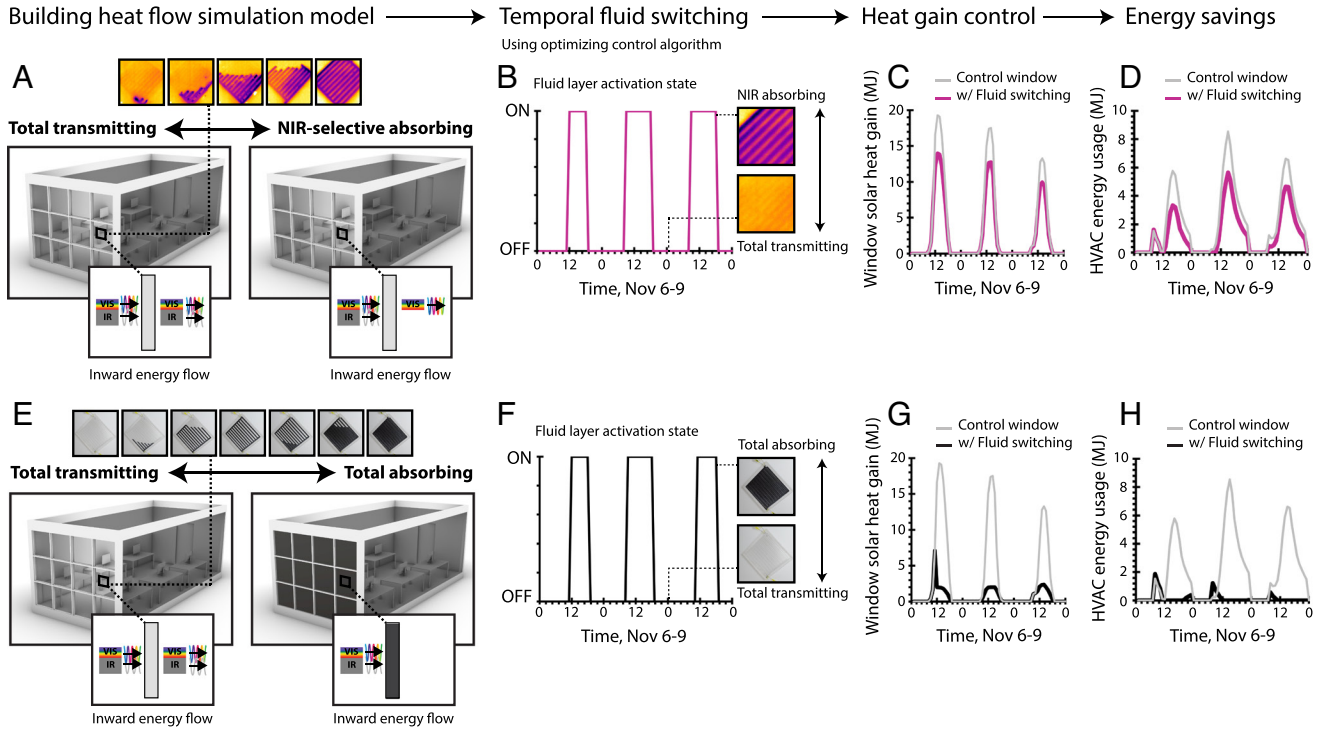

Fig. 5. Simulated solar heat gain tunability. (*A*) Building heat flow model, where heating and cooling energy is calculated based on desired indoor temperature and solar ingress at hourly timesteps, for a switchable NIR-selective absorbing fluid layer. (*B*) Sampled control schedule for activating NIR-selective absorbing layer within glazing to optimize heating and cooling light energy, shown between Nov 6 and 9 of the annual simulation. The model can toggle between two states (NIR absorbing and total transmitting, respective optical properties in Fig. 2*E*). (*C*) Sampled window solar heat gain calculated by model, between Nov 6 and 9, given by dynamic solar control schedule shown in (*B*). (*D*) Sampled heating and cooling energy usage calculated by model, between Nov 6 and 9, given by dynamic solar heating shown in (*C*). Total annual savings are 25%. Full model details explained in *SI Appendix*. (*E*) Building heat flow model, where heating and cooling energy is calculated based on desired indoor temperature and solar ingress at hourly timesteps, for a switchable totally (visible and NIR) absorbing fluid layer. (*F*) Sampled control schedule for activating totally absorbing layer within glazing to optimize heating and cooling light energy, shown between Nov 6 and 9 of the annual simulation. The model can toggle between two states (totally absorbing and totally transmitting, respective optical properties in Fig. 3*E*). (*G*) Sampled window solar heat gain calculated by model, between Nov 6 and 9, given by dynamic solar control schedule shown in (*F*). (*H*) Sampled heating and cooling energy usage calculated by model, between Nov 6 and 9, given by dynamic solar heating shown in (*G*). Total annual savings are 51%. Full model details explained in *SI Appendix*.

ref. 56). We modeled the EC window to switch between four standard states, the RS between two standard states (up and down), and our fluid multilayer to switch between all combinatorial possibilities of 16 total fluids across three distinct layers (all base state optical properties in Fig. 6*B*). To appropriately account for building integration, the RS was modeled on the interior, while the EC and fluid systems were modeled on the exterior, of a standard double-pane window. The zone details, temperature setpoints, and material properties are described in *SI Appendix*.

Because the fluid multilayer can decouple NIR heat gain from visible light transmission (unlike the EC and RS systems), its thermal performance can be controlled while simultaneously optimizing for desired daylighting. We found that, due to this increased state versatility, the fluid multilayer reduced annual electric lighting energy requirements by an estimated 21% and 24% over EC and RS systems, respectively (Fig. 6*F*). In the winter months, due to an increased capacity for solar heat gain, the fluid multilayer also saved an estimated 40% on space-heating energy, and 20% overall, compared with the EC window (Fig. 6*D*). While, in the summer months, due to an increased capacity for NIR-selective absorption, the fluid multilayer saved an estimated 49% on space-cooling energy, and 14% overall, compared with a RS (Fig. 6*E*). Because the static window, however, is not subjected to the same minimum daylighting and glare constraints of a control algorithm, its performance is not easily directly compared.

Operationally, if we adjust the control algorithm to allow for spatial overlighting (>3,000 lux) above 10% within the space, the fluid multilayer will be able to fully leverage its 95% control over total absorption and its 70% control over NIR-selective absorption to increase solar flux and decrease indoor heating loads when energetically favorable. Because EC windows and RSs (when in their binary down state) are restricted by low solar heat gain, this change in operational control increases heating energy reductions by the fluid multilayer to more than 75% and 34% over EC and RS systems, respectively (Fig. 6*D*), corresponding to total energy savings of more than 43% and 36% (Fig. 6*G*). This energetic performance improvement suggests that the interplay between operational control and functional capacity will be crucial toward achieving optimal performance.

Discussion

We have developed a multilayer fluidic architecture for designing and tuning a building's optical response, achieving independent and combinatorial control of spectrally selective visible color

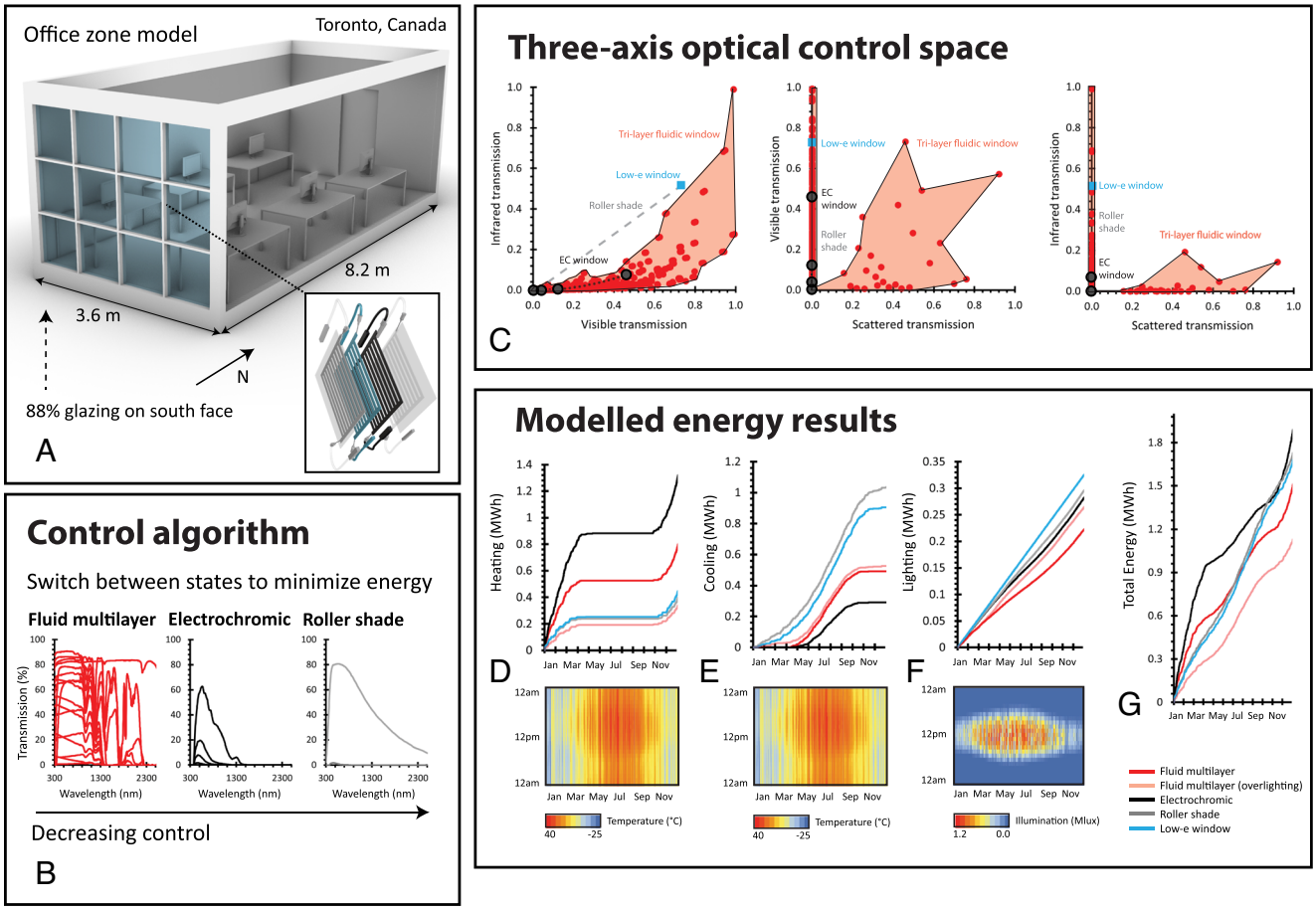

Fig. 6. Fluid multilayer energy savings due to combinatorial optical tunability. (*A*) Reference office model for energy simulations (one-zone). Wall and roof elements are translucent only for illustrative clarity. (*B*) Demonstration of optical property range through which standard control algorithm can switch between, for fluid multilayer, EC, and RS systems. The fluid multilayer can switch between all combinations of the displayed spectral properties due to its multilayered nature. (*C*) Parameter space of all fluid combinations across specular visible (350 to 750 nm), specular (near)-infrared (750 to 2,500 nm), and diffuse visible (350 to 750 nm) optical properties, without considering the optical properties of the double-pane window that was added to the multilayer in simulations. A static low-e window can only address a single point in our control space. EC and RS systems can only address a curve in our control space. Our fluid multilayer can address a volume, across all three axes of our control space. Fluid multilayer (red) points represent all combinations of 16 base states from (*B*). (*D*–*F*) Simulated cumulative heating, cooling, and electric lighting energy for fluid multilayer (both with limited and unlimited spatial overlighting), EC window, RS, and low-e window across annual cycle. Data below illustrates hourly temperature and normal direct solar illumination across the year in Toronto, Canada (simulation environment). (*G*) Total simulated cumulative annual energy data for all described systems, demonstrating superior energy performance by fluid multilayer.

absorption (between 350 and 750 nm), spectrally selective NIR absorption (between 750 and 2,500 nm), total light absorption (between 350 and 2,500 nm), and directional light scattering. This work demonstrates great potential for a scalable "macrofluidic" mechanism within building facades, whereby nontoxic, replenishable, largely recyclable, and easily accessible aqueous fluids confined within overlapping solid layers can be manipulated and switched across large two-dimensional surface areas (0.067 mL/cm^2 or 61 mL/ft^2) to perform a significant number of tunable optical responses. In simulation, we showed that fluid-based scattering could reduce electric lighting consumption by 10%; control over total absorption and NIR-selective absorption could reduce heating and cooling energy by 51% and 25%, respectively; and dynamically optimized combinations of a totally absorbing, NIR-absorbing, and scattering fluid layer throughout the year could outperform a state-of-the-art electrochromic window by 43%.

Analogous to organism physiology, treating building "skin" functions individually allows us to curate the optical conditions within a local indoor environment. Like an additive filtration system, the absorption and reflection spectra of incident light can be dynamically tuned through the activation of sequential fluid layers, each with a specific transmission peak or scattering distribution. The use of nontoxic and replenishable aqueous solutions is important, particularly in comparison to technologies such as electrochromic layers, which require semiconductor fabrication techniques, and toxic materials such as indium tin oxide.

Through bottom-up design of chemical composition, the optical properties of confined fluids (solutions or suspensions) are highly tunable in spectral absorption and scattering. Moreover, liquids and gasses are easily "transportable." As a result of this combined functionality, fluid-based systems can perform a wide range of dynamic optical responses that solid-state materials simply cannot achieve. For example, inorganic oxide-based low-emissivity coatings, chalcogenides and redox-active materials can achieve well-defined optical absorption, but either not dynamically or not with independent control of shading, scattering, and NIR-selective transmission. We suggest that solution-based organic synthesis and nanoparticle suspension chemistry, alternatively, can accomplish an incredible diversity of selective photonic functions. We envision, for example, that buildings might behave as switchable greenhouses, able to admit visible and NIR sunlight in the day, but, through a directed switching of IR-absorbent liquid, block long-wave IR egress in the night. Switchable fluidic NIR and IR responses might be achieved through bottom-up organic synthesis of selectively absorbing and luminescent solar concentrator dyes (85, 86), as well as cholesteric liquid crystalline broadband NIR reflector molecules (87) (summarized well in ref. 4).

There also exists scope for more advanced photonic engineering, where colloidal nanoparticles can be customized to achieve various degrees of specular reflection and scattering, and the bandgap of quantum dot nanocrystals can be tuned to achieve bespoke absorption and emission (88). Colloidal suspensions might also be designed as waveguides—typically achieved using absorption and remission (24, 89), rather than scattering—for building-integrated solar concentration and photovoltaic technologies. Finally, building surfaces containing chemistries with selective visible absorption spectra might be used to mediate human photobiology. Fluids that selectively filter specific visible wavelengths could be dispersed along the facade to achieve on-demand color-change in response to occupant circadian dynamics, with demonstrated potential to improve human alertness, comfort, and overall health (90–92). For example, blue-enriched light (93) has been associated with circadian phase resetting in the morning (94) and increased alertness (90), productivity (95), and cognition (96) during the daytime waking hours. In climates with daylight into the late evening, daylight suppresses melatonin production (91) and delays circadian phase (97); therefore, transmitting longer, less-blue wavelengths would be beneficial. This broad optical programmability, from organic synthesis to photonic particle control, would allow engineers, architects, and chemists to collectively design a building's toolkit of functional responses.

Confined fluids can also be tweaked to improve functionality within real building environments. In colder climates, where glazing-integrated fluids might be exposed to temperatures of −20 °C, low melting-point liquids (ethanol) can be added to aqueous solutions to avoid freezing. This designed functionality can also be coupled with strategic glazing integration (*SI Appendix*, Fig. S9). In the summer, for instance, NIR-absorbing layers are most practical on the exterior of a double-pane window, where absorbed NIR sunlight can be predominantly shed to the outdoors (*SI Appendix*, Fig. S8 provides information on the annual energetic impact of solar absorption and dissipation, while *SI Appendix*, Fig. S10 provides information on the thermal expansion of an aqueous liquid layer across the year). In the winter, however, a NIR-absorbing layer might be beneficial on the interior of a double-pane window, where absorbed sunlight can be convectively transferred indoors. Operationally, different fluid layers might best be integrated on the interior or exterior of an existing glazing unit, while microelectronic components (controller and pump) and fluid reservoirs might be housed within existing window-frame constructions. The focus of this work has been to demonstrate the function, optical tunability, and simulated performance of multilayered devices themselves. There will be issues regarding reservoir storage and fluidic management that could be addressed for the scale up to a meter-size system.

To begin this assessment, we used experimental pumping energy data and simulated layer switching data to estimate the annual cost to operate a 0.10 m^2 trilayer fluidic device (full details in *SI Appendix*). We found that estimated operational energy savings (548 kWh) far exceeded operational energy costs (12.1 kWh) and, estimating device fabrication and implementation costs ($100 USD/$m^2$), resulted in an estimated payback time of roughly 2 y (*SI Appendix*). Of course, more powerful pumps will be required for controlling fluid within larger panels with greater channel heights. A more thorough technoeconomic assessment could be developed to find the optimal digital pump and panel size, to further minimize operational energy costs.

Additionally, this digital control of our dynamic facade is a critical requirement for energy optimization, enabling artificial intelligence for further enhanced building operational efficiency. Deep and reinforcement learning techniques (98–101) can be used to synthesize large amounts of real-time data, better predict occupant and environmental behaviors, and minimize operational energy usage, toward automating a building's multilayered fluidic response. While buildings are becoming increasingly sensory (102–104), the capabilities of existing building facades to respond to high-resolution environmental data are limited, and thus limiting. Our optically reconfigurable system, coupled with internet-of-things (IoT) sensing and data processing technologies, should help advance the smart building paradigm, enabling future generations of buildings to learn.

Finally, in practice, this active fluidic facade should help shift the opto- and thermoregulatory responsibility from centralized mechanical systems within the building core (HVAC), to material systems at the building face. Replacing reactionary systems that postcondition the indoor environment (e.g., interior air conditioners, heaters, and electric lights) with preventative systems that precondition the indoor environment (i.e., our multilayered system of fluids) can cut

heating, cooling, and lighting loads nearly in half, significantly reducing the required size of mechanical systems in residential and commercial spaces, and the total energy needs in urban areas. The potential for this large drop in end-use power consumption may have implications for the way we design buildings, power grids, and, more broadly, the entirety of our urban infrastructure. Our optically general platform introduces a scalable and sustainable path toward achieving energy neutrality in the modern world.

Materials and Methods

Device Fabrication. Multilayered transparent millifluidic devices (15 × 15 × 2 cm^3) were fabricated from stacked 3-mm-thick PMMA sheets (Johnston Industrial Plastics). Channel architectures (1.5 mm deep and 6.35 mm wide) within PMMA layers were milled using a three-axis CNC-mill (AXYZ Pacer 4010 ATC). PMMA layers were adhered using the vapor-polishing technique illustrated in *SI Appendix*, Fig. S1 and described in ref. 105. A needle was sealed to each channel opening using epoxy resin.

Fluid Preparation and Switching. Castor oil (Heritage Store), mineral oil (Howard), and glycerol (99%, BioShop) and polydimethylsiloxane (PDMS) silicone oil (E200 Fluid, 10 cs, ESCO) were used without further purification. Carbon black powder (Davis Colors, 75-μm spherical particles) and P25 titania particles (10 to 40 nm, average particle diameter of 20 nm, ACS Material) were used to generate colloidal suspensions. All suspensions were prepared using deionized water, and were sonicated (iSonic D3200) for 120 s. The PMMA suspensions (average particle diameter of 275 nm, Fig. 3*G*, top image) were synthesized using standard emulsion polymerization methods. Aqueous color dyes were obtained from Club House. Flow to each layer was generated with a NE-1010 digital syringe pump, or, alternatively, with a 12 V direct current digital peristaltic pump (INTLLAB RS385-635). The ends of each channel were connected to small liquid reservoirs/syringes (14 mL) using polyvinyl chloride tubing (1/4″ I.D., 3/8″ O.D.).

Thermal Imaging and Optical/Thermal Measurements. During experimentation, PMMA surface temperature was measured with a k-type thermocouple, fixed onto the PMMA surface. In the experimental setup (Fig. 2*G*), the room that housed the PMMA plate was well-ventilated, to primarily measure radiative heating effects. We used a 100-W incandescent light bulb as a steady-state incident light and heat source. The incandescent light bulb was placed a distance of 8 cms normal to the windowpane, which itself was situated 3 cms in front of the k-type thermocouple (0.523 kJ/kgK) and PMMA sheet (1.42 kJ/kgK). IR images were taken using a FLIR E6-XT infrared camera. UV-vis-infrared spectrophotometry was performed for all fluids using a Perkin-Elmer Lambda 1050 spectrophotometer. Additive fluid spectrophotometry was performed using a Type 25A 10-mm Quartz tandem (divided) cuvette (FireflySci). Light intensity was measured using an Extech HD450 Light Meter Datalogger.

Data, Materials, and Software Availability. All study data are included in the article and/or *SI Appendix*.

ACKNOWLEDGMENTS. We acknowledge the help of Nicholas Hoban and Paul Kozak for providing device fabrication assistance. We also thank Mathias Kolle for providing advice on optical experimentation techniques. Funding: Canadian Foundation for Innovation (CFI) #31799 (B.D.H.). Percy Edward Hart Professorship, University of Toronto (B.D.H.). R.K. was supported by a Canada Graduate Scholarship, a C.W. Bowman Graduate Scholarship, a Bert Wasmund Graduate Fellowship, and a Hatch Graduate Scholarship.

1. O. Edenhofer, *Climate Change 2014: Mitigation of Climate Change* (Cambridge University Press, 2015), **vol. 3**.
2. International Energy Agency, *CO2 Status Report 2017* (IEA, Paris, France, 2018).
3. International Energy Agency, *The Future of Cooling: Opportunities for Energy-Efficient Air Conditioning* (IEA, Paris, France, 2018).
4. H. Khandelwal, A. P. H. J. Schenning, M. G. Debije, Infrared regulating smart window based on organic materials. *Adv. Energy Mater.* **7**, 1602209 (2017), 10.1002/aenm.201602209.
5. N. Lechner, *Heating, Cooling, Lighting: Sustainable Design Methods for Architects* (John Wiley & Sons, 2014).
6. R. C. G. M. Loonen, M. Trčka, D. Cóstola, J. L. M. Hensen, Climate adaptive building shells: State-of-the-art and future challenges. *Renew. Sustain. Energy Rev.* **25**, 483–493 (2013), 10.1016/j.rser.2013.04.016.
7. E. S. Lee, D. L. DiBartolomeo, S. E. Selkowitz, Thermal and daylighting performance of an automated venetian blind and lighting system in a full-scale private office. *Energy Build.* **29**, 47–63 (1998), 10.1016/S0378-7788(98)00035-8.
8. C.-A. Pan, T. Jeng, Cellular robotic architecture. *Int. J. Archit. Comput.* **10**, 319–339 (2012), 10.1260/1478-0771.10.3.319.
9. S. Attia, Evaluation of adaptive facades: The case study of Al Bahr Towers in the UAE. *QScience Connect* **2017** (2018), http://dx.doi.org/10.5339/connect.2017.qgbc.6.
10. J. Lienhard *et al.*, Flectofin: A hingeless flapping mechanism inspired by nature. *Bioinspir. Biomim.* **6**, 045001 (2011), 10.1088/1748-3182/6/4/045001.
11. Z. Drozdowski, S. Gupta, Adaptive Fritting as Case Exploration for Adaptivity in Architecture, Proceedings of the 29th Annual Conference of the Association for Computer Aided Design in Architecture (ACADIA), Chicago (Illinois) 22-25 October (2009), pp. 105–109. https://doi.org/10.52842/conf.acadia.2009.105.
12. D. Park *et al.*, Dynamic daylight control system implementing thin cast arrays of polydimethylsiloxane-based millimeter-scale transparent louvers. *Build. Environ.* **82**, 87–96 (2014), 10.1016/j.buildenv.2014.07.016.
13. A. K. Elizabeth, I. S. Shane, H. D. Anna, "Dynamic window daylighting systems: electropolymeric technology for solar responsive building envelopes", Proc. SPIE 7976, Electroactive Polymer Actuators and Devices (EAPAD) 2011, 79763A. https://doi.org/10.1117/12.885720. Accessed 29 March 2011.
14. D. M. Wood, D. Correa, O. D. Krieg, A. Menges, Material computation–4D timber construction: Towards building-scale hygroscopic actuated, self-constructing timber surfaces. *Int. J. Archit. Comput.* **14**, 49–62 (2016), 10.1177/1478077115625522.
15. S. Reichert, A. Menges, D. Correa, Meteorosensitive architecture: Biomimetic building skins based on materially embedded and hygroscopically enabled responsiveness. *Comput.-Aided Des.* **60**, 50–69 (2015), 10.1016/j.cad.2014.02.010.
16. J. Grinham, R. Blabolil, J. Haak, Harvest Shade Screens: Programming material for optimal energy building skins, Proceedings of the 34th Annual Conference of the Association for Computer Aided Design in Architecture (ACADIA), Los Angeles 23-25 October, 2014), pp. 281–290. https://doi.org/10.52842/conf.acadia.2014.281.
17. D. Ge *et al.*, A robust smart window: Reversibly switching from high transparency to angle-independent structural color display. *Adv. Mater.* **27**, 2489–2495 (2015), 10.1002/adma.201500281.
18. P. Van Konynenburg, S. Marsland, J. McCoy, Solar radiation control using NCAP liquid crystal technology. *Sol. Energy Mater.* **19**, 27–41 (1989), 10.1016/0165-1633(89)90021-X.
19. P. S. Drzaic, Polymer dispersed nematic liquid crystal for large area displays and light valves. *J. Appl. Phys.* **60**, 2142–2148 (1986), 10.1063/1.337167.
20. D. Cupelli *et al.*, Self-adjusting smart windows based on polymer-dispersed liquid crystals. *Sol. Energy Mater. Sol. Cells* **93**, 2008–2012 (2009), 10.1016/j.solmat.2009.08.002.
21. A. Ghosh, B. Norton, A. Duffy, Daylighting performance and glare calculation of a suspended particle device switchable glazing. *Solar Energy* **132**, 114–128 (2016), 10.1016/j.solener.2016.02.051.
22. R. Vergaz, J.-M. Sánchez-Pena, D. Barrios, C. Vázquez, P. Contreras-Lallana, Modelling and electro-optical testing of suspended particle devices. *Sol. Energy Mater. Sol. Cells* **92**, 1483–1487 (2008), 10.1016/j.solmat.2008.06.018.
23. R. Vergaz, J. Pena, D. Barrios, I. Pérez, J. Torres, Electrooptical behaviour and control of a suspended particle device. *Opto-Electron. Rev.* **15**, 154–158 (2007), 10.2478/s11772-007-0013-9.
24. M. G. Debije, Solar energy collectors with tunable transmission. *Adv. Funct. Mater.* **20**, 1498–1502 (2010), 10.1002/adfm.200902403.
25. N. DeForest, A. Shehabi, S. Selkowitz, D. J. Milliron, A comparative energy analysis of three electrochromic glazing technologies in commercial and residential buildings. *Appl. Energy* **192**, 95–109 (2017), 10.1016/j.apenergy.2017.02.007.
26. C. G. Granqvist, P. C. Lansåker, N. R. Mlyuka, G. A. Niklasson, E. Avendaño, Progress in chromogenics: New results for electrochromic and thermochromic materials and devices. *Sol. Energy Mater. Sol. Cells* **93**, 2032–2039 (2009), 10.1016/j.solmat.2009.02.026.
27. D. Cupelli, F. P. Nicoletta, S. Manfredi, G. D. Filpo, G. Chidichimo, Electrically switchable chromogenic materials for external glazing. *Sol. Energy Mater. Sol. Cells* **93**, 329–333 (2009), 10.1016/j.solmat.2008.11.010.
28. C. M. Lampert, Chromogenic smart materials. *Mater. Today* **7**, 28–35 (2004), 10.1016/S1369-7021(04)00123-3.
29. C. G. Granqvist, Chromogenic materials for transmittance control of large-area windows. *Crit. Rev. Solid State Mater. Sci.* **16**, 291–308 (1990), 10.1080/10408439008242184.
30. E. S. Lee, D. L. DiBartolomeo, Application issues for large-area electrochromic windows in commercial buildings. *Sol. Energy Mater. Solar Cells* **71**, 465–491 (2002), 10.1016/S0927-0248(01)00101-5.
31. Y. Wang, E. L. Runnerstrom, D. J. Milliron, Switchable materials for smart windows. *Annu. Rev. Chem. Biomol. Eng.* **7**, 283–304 (2016), 10.1146/annurev-chembioeng-080615-034647.
32. J. García-Cañadas, A. P. Meacham, L. M. Peter, M. D. Ward, A near-infrared electrochromic window based on an Sb-doped SnO2 electrode modified with a Ru–dioxolene complex. *Angew. Chem.* **115**, 3119–3122 (2003).
33. J. Niu *et al.*, Infrared electrochromic materials, devices and applications. *Appl. Mater. Today* **24**, 101073 (2021), 10.1016/j.apmt.2021.101073.
34. G. Garcia *et al.*, Dynamically modulating the surface plasmon resonance of doped semiconductor nanocrystals. *Nano Lett.* **11**, 4415–4420 (2011), 10.1021/nl202597n.
35. C. G. Granqvist, Transparent conductors as solar energy materials: A panoramic review. *Sol. Energy Mater. Sol. Cells* **91**, 1529–1598 (2007), 10.1016/j.solmat.2007.04.031.
36. X.-H. Li, C. Liu, S.-P. Feng, N. X. Fang, Broadband Light Management with Thermochromic Hydrogel Microparticles for Smart Windows. *Joule* **3**, 290–302 (2019), 10.1016/j.joule.2018.10.019.
37. C. Yu *et al.*, Adaptive optoelectronic camouflage systems with designs inspired by cephalopod skins. *Proc. Natl. Acad. Sci. U.S.A.* **111**, 12998–13003 (2014), 10.1073/pnas.1410494111.
38. N. DeForest *et al.*, United States energy and CO2 savings potential from deployment of near-infrared electrochromic window glazings. *Build. Environ.* **89**, 107–117 (2015), 10.1016/j.buildenv.2015.02.021.

39. S. Craig, J. Grinham, Breathing walls: The design of porous materials for heat exchange and decentralized ventilation. *Energy Build.* **149**, 246–259 (2017), 10.1016/j.enbuild.2017.05.036.
40. E. S. Stephen, S. L. Eleanor, A. Øyvind, "Perspectives on advanced facades with dynamic glazings and integrated lighting controls." *CISBAT, Lusanne, Switzarland (2003).66: National Fenestration Rating Council, Inc. Therm 7/Window 7 NFRC Simulation Manual*. Available online: https://windows.lbl.gov/sites/default/files/Downloads/NFRCSim7-July2017.pdf (Accessed 10 July 2021).
41. L. Pérez-Lombard, J. Ortiz, C. Pout, A review on buildings energy consumption information. *Energy Build.* **40**, 394–398 (2008), 10.1016/j.enbuild.2007.03.007.
42. A. Llordés, G. Garcia, J. Gazquez, D. J. Milliron, Tunable near-infrared and visible-light transmittance in nanocrystal-in-glass composites. *Nature* **500**, 323–326 (2013), 10.1038/nature12398.
43. J. B. Messenger, Cephalopod chromatophores: Neurobiology and natural history. *Biol. Rev. Camb. Philos. Soc.* **76**, 473–528 (2001), 10.1017/s1464793101005772.
44. R. L. Sutherland, L. M. Mäthger, R. T. Hanlon, A. M. Urbas, M. O. Stone, Cephalopod coloration model. II. Multiple layer skin effects. *J. Opt. Soc. Am. A. Opt. Image Sci. Vis.* **25**, 2044–2054 (2008), 10.1364/josaa.25.002044.
45. R. T. Hanlon *et al.*, Cephalopod dynamic camouflage: Bridging the continuum between background matching and disruptive coloration. *Philos. Trans. R. Soc. Lond. B. Biol. Sci.* **364**, 429–437 (2009), 10.1098/rstb.2008.0270.
46. L. F. Deravi *et al.*, The structure-function relationships of a natural nanoscale photonic device in cuttlefish chromatophores. *J. R. Soc. Interface* **11**, 20130942–20130942 (2014), 10.1098/rsif.2013.0942.
47. L. M. Mäthger, R. T. Hanlon, Malleable skin coloration in cephalopods: Selective reflectance, transmission and absorbance of light by chromatophores and iridophores. *Cell Tissue Res.* **329**, 179 (2007), 10.1007/s00441-007-0384-8.
48. L. M. Mäthger, E. J. Denton, N. J. Marshall, R. T. Hanlon, Mechanisms and behavioural functions of structural coloration in cephalopods. *J. R. Soc. Interface* **6**, S149–S163 (2009), 10.1098/rsif.2008.0366.focus.
49. T. J. Wardill, P. T. Gonzalez-Bellido, R. J. Crook, R. T. Hanlon, Hanlon, neural control of tuneable skin iridescence in squid. *Proc. Biol. Sci.* **279**, 4243–4252 (2012), 10.1098/rspb.2012.1374.
50. D. E. Morse, E. Taxon, Reflectin needs its intensity amplifier: Realizing the potential of tunable structural biophotonics. *Appl. Phys. Lett.* **117**, 220501 (2020), 10.1063/5.0026546.
51. J. Teyssier, S. V. Saenko, D. van der Marel, M. C. Milinkovitch, Photonic crystals cause active colour change in chameleons. *Nat. Commun.* **6**, 6368 (2015), 10.1038/ncomms7368.
52. Ethan Daniels & Alamy Stock Photo, *A Bigfin reef squid. Image ID: R17EGR*. https://www.alamy.com/a-bigfin-reef-squid-sepioteuthis-lessoniana-hovers-in-the-dark-waters-of-the-western-pacific-ocean-near-a-coral-reef-in-indonesia-image224514551.html?imageid=9F915008-2E85-4F92-AD7F-7D89B5281315&p=38727&pn=1&searchId=efc1c32313afe1c8e478586bbc9216d6&searchtype=0. Accessed 23 May 2017.
53. Ethan Daniels & Alamy Stock Photo, *A Bigfin reef squid. Image ID: JEMRHC*. https://www.alamy.com/stock-photo-a-bigfin-reef-squid-sepioteuthis-lessoniana-hovers-in-nighttime-waters-146745688.html?p=38727. Accessed 10 August 2022.
54. R. Kay, C. Katrycz, K. Nitièma, J. A. Jakubiec, B. D. Hatton, Decapod-inspired pigment modulation for active building facades. *Nat. Commun.* **13**, 4120 (2022), 10.1038/s41467-022-31527-6.
55. B. D. Hatton *et al.*, An artificial vasculature for adaptive thermal control of windows. *Sol. Energy Mater. Sol. Cells* **117**, 429–436 (2013), 10.1016/j.solmat.2013.06.027.
56. R. Kay *et al.*, Shape-programmable fluid bubbles for responsive building skins. *J. Build. Eng.* **48**, 103942 (2022), 10.1016/j.jobe.2021.103942.
57. R. Kay, C. W. Katrycz, E. J. Heimlich, B. D. Hatton, Hatton, programmable droplets: Leveraging digitally-responsive flow fields to actively tune liquid morphologies. *PLoS One* **17**, e0264141 (2022), 10.1371/journal.pone.0264141.
58. H. Mor, *et al.*, in *Proceedings of the 2020 CHI Conference on Human Factors in Computing Systems 1–14* (Association for Computing Machinery, Honolulu, HI, 2020).
59. S. A. Morin *et al.*, Camouflage and display for soft machines. *Science* **337**, 828–832 (2012), 10.1126/science.1222149.
60. A. B. Theberge *et al.*, Microdroplets in microfluidics: An evolving platform for discoveries in chemistry and biology. *Angew. Chem. Int. Ed. Engl.* **49**, 5846–5868 (2010).
61. K. i. Ohno, K. Tachikawa, A. Manz, Microfluidics: Applications for analytical purposes in chemistry and biochemistry. *Electrophoresis* **29**, 4443–4453 (2008).
62. A. Burklund, A. Tadimety, Y. Nie, N. Hao, J. X. Zhang, Advances in diagnostic microfluidics. *Adv. Clin. Chem.* **95**, 1–72 (2020).
63. P. Yager *et al.*, Microfluidic diagnostic technologies for global public health. *Nature* **442**, 412–418 (2006).
64. M. Prakash, N. Gershenfeld, Microfluidic bubble logic. *Science* **315**, 832–835 (2007), 10.1126/science.1136907.
65. M. Yafia *et al.*, Microfluidic chain reaction of structurally programmed capillary flow events. *Nature* **605**, 464–469 (2022), 10.1038/s41586-022-04683-4.
66. National Fenestration Rating Council, Therm 7/Window 7 NFRC Simulation Manual. (2017). https://windows.lbl.gov/sites/default/files/Downloads/NFRCSim7-July2017.pdf (Accessed 10 July 2021).
67. J. Karlsson, A. Roos, Annual energy window performance vs. glazing thermal emittance – the relevance of very low emittance values. *Thin Solid Films* **392**, 345–348 (2001), 10.1016/S0040-6090(01)01055-0.
68. R. J. Martín-Palma, Spectrally selective coatings on glass: Solar-control and low-emissivity coatings. *J. Nanophotonics* **3**, 030305 (2009).
69. H. Ye, X. Meng, L. Long, B. Xu, The route to a perfect window. *Renewable Energy* **55**, 448–455 (2013), 10.1016/j.renene.2013.01.003.
70. J. Kim *et al.*, Nanocomposite architecture for rapid, spectrally-selective electrochromic modulation of solar transmittance. *Nano Lett.* **15**, 5574–5579 (2015), 10.1021/acs.nanolett.5b02197.
71. S. Papaefthimiou, E. Syrrakou, P. Yianoulis, Energy performance assessment of an electrochromic window. *Thin Solid Films* **502**, 257–264 (2006), 10.1016/j.tsf.2005.07.294.
72. D. F. Swinehart, The beer-lambert law. *J. Chem Educ.* **39**, 333 (1962).
73. M. Boubekri, N. Cheung Ivy, J. Reid Kathryn, C.-H. Wang, C. Zee Phyllis, Impact of windows and daylight exposure on overall health and sleep quality of office workers: A case-control pilot study. *J. Clin. Sleep Med.* **10**, 603–611 (2014), 10.5664/jcsm.3780.
74. R. G. Hopkinson, Glare from daylighting in buildings. *Appl. Ergon.* **3**, 206–215 (1972), 10.1016/0003-6870(72)90102-0.
75. D. W. Hahn, Light scattering theory (*Department of Mechanical and Aerospace Engineering, University of Florida*, 2009).
76. H. C. Hulst, H. C. van de Hulst, *Light Scattering by Small Particles* (Courier Corporation, 1981).
77. J. W. Strutt LVIII, On the scattering of light by small particles. *London, Edinburgh, and Dublin Philos. Mag. J. Sci.* **41**, 447–454 (1871).
78. K. Krishnamurti, Investigations on the scattering of light in colloidal solutions and gels. Part I. Agar sol and gel. *Proc. R. Soc. Lond. Ser. A. Containing Pap. Math. Phys Charact.* **122**, 76-103 (1929).
79. G. J. Ward, in *Proceedings of the 21st Annual Conference on Computer Graphics and Interactive Techniques* (Association for Computing Machinery, 1994), pp. 459–472.
80. U.S. Department of Energy, EnergyPlus™ Version 9.6.0 Documentation. Engineering Reference. *U.S. Department of Energy*. (2021). https://energyplus.net/assets/nrel_custom/pdfs/pdfs_v9.6.0/EngineeringReference.pdf. Accessed 23 September 2021.
81. C. F. Reinhart, J. A. Jakubiec, D. Ibarra Definition Of A Reference Office For Standardized Evaluations Of Dynamic Facade And Lighting Technologies. 13th Conference of International Building Performance Simulation Association, Chambéry, France, 2013 3645–3652. https://doi.org/10.26868/25222708.2013.1029.
82. J. A. Jakubiec, Validation of Simplified Visual Discomfort Calculations. *Proceedings of BSO 2018: 4th Building Simulation and Optimization Conference*, Cambridge, UK (2018) 17–23.
83. C. Curcija *et al.*, *WINDOW Technical Documentation* (Lawrence Berkeley National Laboratory, 2018).
84. H. Ceylan, G. E. Myers, Long-time solutions to heat-conduction transients with time-dependent inputs. *J. Heat Transfer-Trans. ASME* **102**, 115–120 (1980).
85. W. Zhao, E. M. Carreira, Carreira, conformationally restricted aza-BODIPY: Highly fluorescent, stable near-infrared absorbing dyes. *Chem. A Eur. J.* **12**, 7254–7263 (2006).
86. M. G. Debije, P. P. Verbunt, Verbunt, Thirty years of luminescent solar concentrator research: Solar energy for the built environment. *Adv. Energy Mater.* **2**, 12–35 (2012).
87. X. Chen *et al.*, Broadband reflection of polymer-stabilized chiral nematic liquid crystals induced by a chiral azobenzene compound. *Chem. Commun.* **50**, 691–694 (2014).
88. S. A. McDonald *et al.*, Solution-processed PbS quantum dot infrared photodetectors and photovoltaics. *Nat. Mater.* **4**, 138–142 (2005), 10.1038/nmat1299.
89. F. Meinardi, F. Bruni, S. Brovelli, Luminescent solar concentrators for building-integrated photovoltaics. *Nat. Rev. Mater.* **2**, 17072 (2017), 10.1038/natrevmats.2017.72.
90. C. Cajochen, J. M. Zeitzer, C. A. Czeisler, D. J. Dijk, Dose-response relationship for light intensity and ocular and electroencephalographic correlates of human alertness. *Behav. Brain. Res.* **115**, 75–83 (2000), 10.1016/s0166-4328(00)00236-9.
91. J. J. Gooley *et al.*, Exposure to room light before bedtime suppresses melatonin onset and shortens melatonin duration in humans. *J. Clin. Endocrinol. Metab.* **96**, E463–E472 (2011), 10.1210/jc.2010-2098.
92. R. G. Abeysuriya, S. W. Lockley, P. A. Robinson, S. Postnova, Postnova, A unified model of melatonin, 6-sulfatoxymelatonin, and sleep dynamics. *J. Pineal. Res.* **64**, e12474 (2018), 10.1111/jpi.12474.
93. J. Enezi *et al.*, A "melanopic" spectral efficiency function predicts the sensitivity of melanopsin photoreceptors to polychromatic lights. *J. Biol. Rhythms* **26**, 314–323 (2011), 10.1177/0748730411409719.
94. D. S. Minors, J. M. Waterhouse, A. Wirz-Justice, A human phase-response curve to light. *Neurosci. Lett.* **133**, 36–40 (1991), 10.1016/0304-3940(91)90051-t.
95. S. L. Chellappa *et al.*, Non-visual effects of light on melatonin, alertness and cognitive performance: Can blue-enriched light keep us alert? *PLoS One* **6**, e16429 (2011), 10.1371/journal.pone.0016429.
96. O. Keis, H. B. Helbig, J. Streb, K. Hille, Influence of blue-enriched classroom lighting on students' cognitive performance. *Trends Neurosci. Education* **3**, 86–92 (2014).
97. S. B. Khalsa, M. E. Jewett, C. Cajochen, C. A. Czeisler, A phase response curve to single bright light pulses in human subjects. *J. Physiol.* **549**, 945–952 (2003), 10.1113/jphysiol.2003.040477.
98. I. C. Konstantakopoulos *et al.*, A deep learning and gamification approach to improving human-building interaction and energy efficiency in smart infrastructure. *Appl. Energy* **237**, 810–821 (2019), 10.1016/j.apenergy.2018.12.065.
99. Z. Wang, T. Hong, Reinforcement learning for building controls: The opportunities and challenges. *Appl. Energy* **269**, 115036(2020), 10.1016/j.apenergy.2020.115036.
100. K. Dalamagkidis, D. Kolokotsa, K. Kalaitzakis, G. S. Stavrakakis, Reinforcement learning for energy conservation and comfort in buildings. *Build. Environ.* **42**, 2686–2698 (2007), 10.1016/j.buildenv.2006.07.010.
101. M. Han *et al.*, A review of reinforcement learning methodologies for controlling occupant comfort in buildings. *Sustainable Cities Soc.* **51**, 101748 (2019), 10.1016/j.scs.2019.101748.
102. M. Manic, D. Wijayasekara, K. Amarasinghe, J. J. Rodriguez-Andina, Building energy management systems: The age of intelligent and adaptive buildings. *IEEE Ind. Electron. Mag.* **10**, 25–39 (2016), 10.1109/MIE.2015.2513749.
103. B. Dong, V. Prakash, F. Feng, Z. O'Neill, A review of smart building sensing system for better indoor environment control. *Energy Build.* **199**, 29–46 (2019).
104. A. Verma, S. Prakash, V. Srivastava, A. Kumar, S. C. Mukhopadhyay, Sensing, controlling, and IoT infrastructure in smart building: A review. *IEEE Sensors J.* **19**, 9036–9046 (2019).
105. I. R. G. Ogilvie *et al.*, "Solvent processing of PMMA and COC chips for bonding devices with optical quality surfaces" in 14th International Conference on Miniaturized Systems for Chemistry and Life Sciences, S. Verpoorte, J. Emneus, H. Andersson-Svahn, N. Pamme, Eds. (Curran Associates, Inc., Red Hook, NY, 2010), pp. 1244–1246.